Exploring Configurations of Nanocrystal Ligands Using Machine-Learned Force Fields

Jakub K. Sowa,[*,†,¶] Sean T. Roberts,[‡,¶] and Peter J. Rossky[*,†,¶]

†*Department of Chemistry, Rice University, Houston, Texas 77005, USA*

‡*Department of Chemistry, The University of Texas at Austin, Austin, Texas 78712, USA*

¶*Center for Adapting Flaws into Features, Rice University, Houston, Texas 77005, USA*

E-mail: jakub.sowa@oxon.org; peter.rossky@rice.edu

Abstract

Semiconducting nanocrystals passivated with organic ligands have emerged as a powerful platform for light harvesting, light-driven chemical reactions, and sensing. Due to their complexity and size, little structural information is available from experiments, making these systems challenging to model computationally. Here, we develop a machine-learned force field trained on DFT data and use it to investigate surface chemistry of a PbS nanocrystal interfaced with acetate ligands. In doing so, we go beyond considering individual local minimum energy geometries and, importantly, circumvent a precarious issue associated with the assumption of a single assigned atomic partial charge, for each element in a nanocrystal, independent of its structural position. We demonstrate that the carboxylate ligands passivate the metal-rich surfaces by adopting a very wide range of 'tilted-bridge' and 'bridge' geometries and investigate the corresponding ligand IR spectrum. This work illustrates the potential of machine-learned force fields to transform computational modelling of these materials.

TOC Graphic

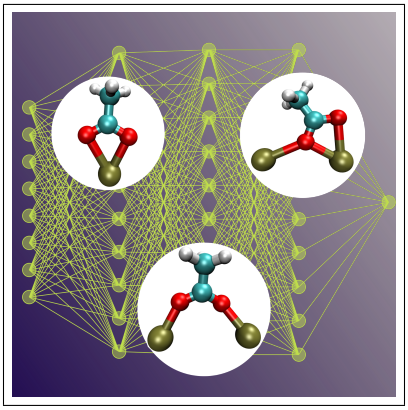

Colloidal nanocrystals are attractive materials for optoelectronic devices and sensors due to their tunable light absorption properties and high molar extinction coefficients.[1,2] Such semiconducting nanocrystals, or quantum dots (QD), are typically passivated with organic ligands which stabilise them chemically[3–5] and can not only influence their optoelectronic properties[6–9] but also constitute key components in QD-based devices, for instance, as charge or energy acceptors.[10,11] The details of the surface chemistry at the semiconducting-organic interface are therefore crucial to the performance of nanocrystal-based technologies.[12]

Experimental investigations of the structure of these interfaces are challenging due to the complexity and heterogeneity of colloidal nanocrystals. Hence, computational modelling of such QDs is an attractive research approach but is more demanding when realistically interfaced with organic ligands. Typically, the geometries of these systems are obtained by DFT-based geometry optimization.[13–19] Such calculations are particularly computationally intensive due to the sheer number of degrees of freedom and the resulting size of the conformational space. Because of the number of possible energy minima, the outputs of these calculations will, for instance, frequently depend on the initial geometry.[20] Furthermore, it is generally not known if a particular local energy minimum is representative of the distribution of structures present at non-zero temperature.

Alternatively, one can turn to performing molecular dynamics (MD) simulations. This has been done in the past using analytical force fields which explicitly account for the electrostatic, bonding, and van der Waals interactions.[21–27] Such simulations allow for sampling of the geometries present at a desired temperature, as well as for investigating much larger systems, and including explicit solvation. Formulating and validating a conventional molecular mechanics force field is challenging however, in part due to the scarcity of experimental data on an atomic scale. For example, the apparent partial charges on various metal atoms are reasonably expected to depend not only on the stoichiometry of the nanocrystal but also on their position (e.g., at a vertex, at the surface or in the interior of the nanocrystal; see futher discussion below) and on their ligand coordination. Additionally, relevant force

fields may need to allow for the possibility of a covalent component of bonding between the semiconductor and the ligands which are mobile on a surface of the nanocrystal.[28] Consequently, for PbS nanocrystals, for instance, force fields with very different partial-charge and Lennard-Jones parameters have been proposed and used in the literature.[29–32] *Ab initio* MD simulations are capable of alleviating the problems just discussed, but, for the systems of interest, the high computational intensity limits them to relatively short simulation times.[33]

Over the last fifteen years, MD simulations based on machine-learned (ML) force fields have emerged as an effective alternative to *ab initio* MD.[34–38] Within this method, a ML (typically neural-net or kernel-based) algorithm is trained on data obtained from *ab initio* quantum chemical calculations to predict both the energies and forces associated with atomic configurations and this result is then used in Monte Carlo or MD simulations. The sequential evaluation of the total energy and its gradients can normally be accomplished orders of magnitude faster than is possible using *ab initio* electronic structure, allowing for much longer simulations and larger system sizes, as compared to *ab initio* MD.[39–43] Concurrently, ML algorithms can, in principle, approach the accuracy of the quantum chemistry method used to obtain training data and thus offer a substantial advantage over conventional (analytical) force fields. In this work, we develop and make use of neural-net based ML force fields trained on DFT data to further our understanding of the surface chemistry of PbS nanocrystals beyond what can be easily accomplished with conventional methods.

Our model system is shown in the inset of Figure 1. It comprises an ultra-small $Pb_{19}S_6$ nanocrystal with a diameter of 1.2 nm postulated by Choi *et al.* on the basis of their experimental work.[5] This heavily lead-rich quantum dot has a rock-salt-type structure and an octahedral shape with eight (111) surfaces passivated with 26 (de-protonated) carboxylate ligands, making the overall system charge-neutral.[44] In the present test case, the oleate ligands used in the synthesis[1,5] were replaced with acetates for computational expediency. It is generally thought that a PbS nanocrystal with a diameter below 3 nm possesses exclusively lead-rich (111) surfaces.[5,45,46] We believe, therefore, that the considered model system can

also shed light on the behavior of somewhat larger quantum dots such as those used recently to achieve photon upconversion.[47]

To illustrate some of the difficulties that would be associated with using a standard analytical force field here, we briefly consider the atomic partial charges for the model system at hand. We evaluate them using ESP analysis[48] (i.e., by fitting the DFT electrostatic potential). This results in a rather wide distribution of charges for each of the elemental atom types, as displayed in Figure S8. In particular, we find that the partial charges on Pb atoms depend on their position within the nanocrystal: we obtain average values of $0.94e$, $0.72e$, and $0.58e$ for atoms at the edge, vertex or in the interior of the QD, respectively. As discussed above, ML force fields allow us to circumvent the issue of parametrizing atomic partial charges since they do not rely on models that separate the bonding, van der Waals, and electrostatic interactions.

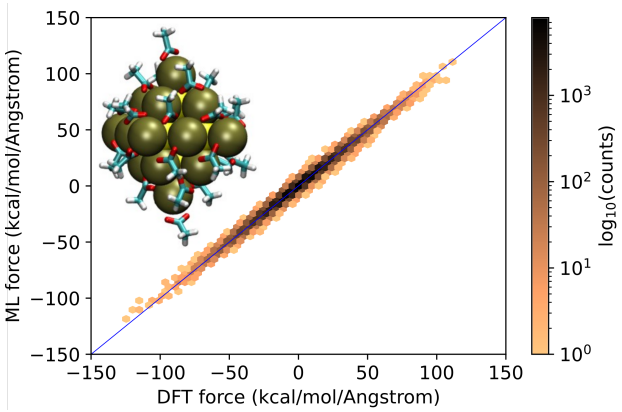

Figure 1: Correlation between the DFT and ML force components sampled every 100 ps during five considered 3 ns runs. Inset: The $Pb_{19}S_6(CH_3COO)_{26}$ model system considered in this work.

The ML force fields in this work were developed with the DeePMD package.[49–51] They were trained on DFT energies and forces using an iterative procedure beginning with a set of geometries obtained using an analytical force field;[31] see the Methods and Section S1 for details. Two types of force fields were considered. In the first, the PbS nanocrystal is assumed frozen in accord with an idealised crystal geometry; this force field will be referred to as FF1. For the second force field, FF2, we removed any constraints from the surface Pb

atoms. Atoms in the interior of the nanocrystal remain fixed throughout. We do not include any effects of a dielectric environment or treat solvent effects in the present study. We make use of the FF2 force field to obtain all the results presented in the main text while those produced using FF1 are discussed in Section S4.

Following the training of the force field, we select 5 geometries from the validation set and use each of them as an initial geometry in an independent 3 ns MD simulation performed at 300 K; see Methods for details. To test the accuracy of the considered force field during the simulations, we evaluate the DFT energies and forces associated with geometries sampled every 100 ps (155 structures in total) and compare them to those predicted by the ML force field. We obtain the mean-absolute error (MAE) and the root-mean-square error (RMSE) on energy of MAE = 3.26 kcal/mol and RMSE = 4.20 kcal/mol (corresponding to 0.68 and 0.88 meV/atom, respectively). The RMSE on force components is found to be 1.82 kcal/mol/Å, comparable to what is usually achieved with ML force fields in the literature.[40,52] In Figure 1, we show the correlation between the predicted ML and calculated DFT force components; the correlation between the ML and DFT energies is shown in Figure S3.

We next analyze the ligand geometries observed during the above simulations. In each run, the first 1 ns is largely relaxation and is disregarded in the analysis. As schematically shown in Figure 2(a), geometries adopted by the carboxylate ligands are usually categorised as belonging to either bridge, chelate, tilted-bridge or unidentate type based on their coordination with metal atoms on the surface of the nanocrystal.[28,53] To understand the ligand binding quantitatively, we perform the following coordination analysis in which we purposefully avoid introducing any specific or arbitrary distance criteria. As schematically illustrated on the example of a tilted-bridge ligand in the inset of Figure 2(b), for each of the ligands, we first identify its "primary" lead atom, Pb*, as the Pb atom closest to the average position of the two oxygen atoms. The two Pb*-O distances are then defined as r_1 and r_2 (where $r_1 < r_2$). The shortest of the Pb-O distances to any Pb atom other than Pb* is defined as r_3. Distance r_1 will correspond to the Pb-O bonding interaction. The relative magnitudes

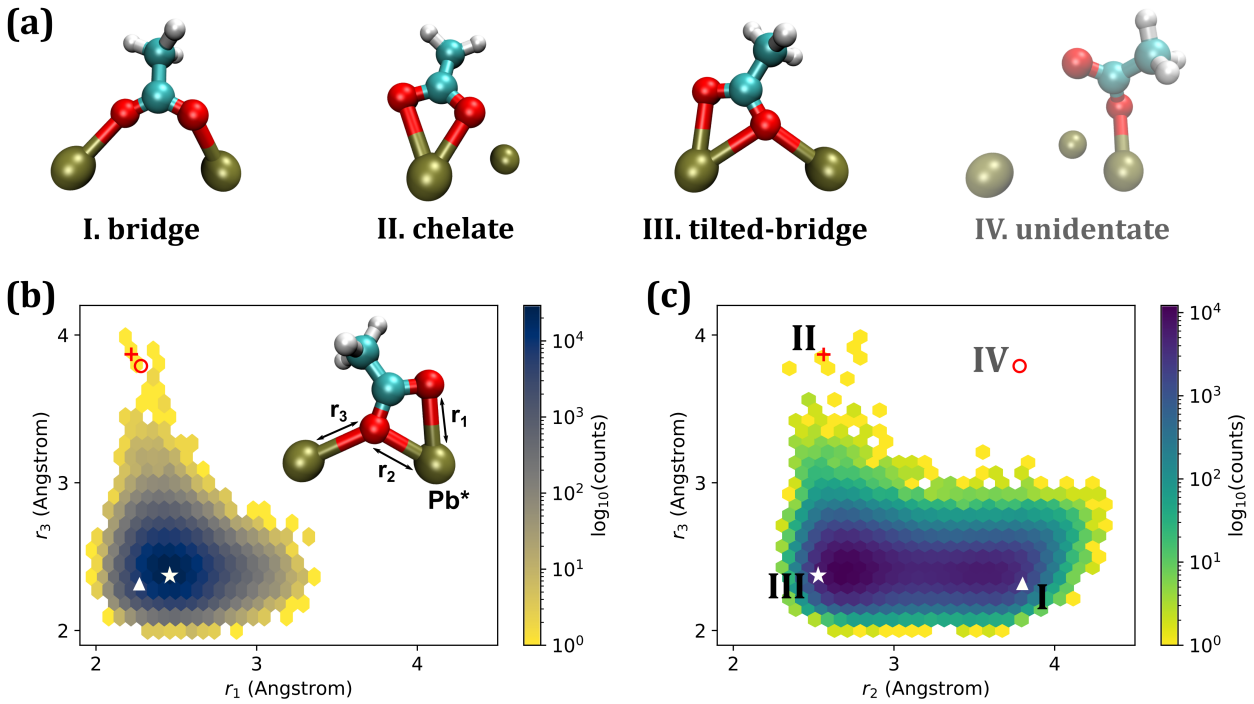

Figure 2: (a) Examples of coordination geometries adopted by the acetate ligands, using descriptive labels suggested in literature.[28,53] Geometries I-III were identified in the simulations. Geometry IV is a hypothetical geometry. (b, c) Histogram plots of (b) r_1 *vs.* r_3 and (c) r_2 *vs.* r_3 distances. Symbols show the r_{1-3} values corresponding to the bridge ($\triangle$), chelate ($+$), tilted-bridge ($\star$), and unidentate ($\circ$) geometries shown in (a). Inset in (b) illustrates the defined distances underlying the classification algorithm used here (see text).

of the r_2 and r_3 however will depend on the coordination geometry of the considered ligand; see Figure 2(a). In particular, for a chelate, one ought to expect a relatively short r_2 and a longer r_3 distance. The reverse is true for a bridge-type coordination where the two Pb-O bonds involve distinct lead atoms. For a tilted-bridge geometry, both r_2 and r_3 should be relatively short (and comparable to r_1) while for a simple unidentate coordination r_2 and r_3 ought to be significantly longer than r_1. These expectations are illustrated by the r_{1-3} values corresponding to the structures shown in Figure 2(a), marked in panels (b) and (c).

In Figure 2(b), we plot a 2D histogram of the r_1 *vs.* r_3 distances. We observe a single broad maximum at around r_1, $r_3 \sim 2.5$ Å indicating that chelating geometries are rarely observed and that ligands typically bridge at least two different Pb atoms, similarly to what has been previously reported in computational studies of passivated CdSe nanocrystals.[28,54]

Additionally, the r_2 *vs.* r_3 histogram in Figure 2(c) reveals the presence of two maxima at around $r_2 = 2.7$ and 3.6 Å, corresponding to the tilted-bridging and bridging geometries, respectively. We note however that the two distributions are very broad and overlap with a surprisingly wide range of coordination geometries apparently accessible at room temperature. Finally, no evidence of unidentate structures is observed for this case in the r_2 *vs.* r_3 histogram. To additionally validate our results, we performed DFT optimizations of 10 nanocrystal geometries sampled from the MD simulations, comprising 260 initial ligand geometries. As discussed in Section S5, the obtained local-minimum geometries comprise a distribution of tilted-bridge and bridge geometries and do not feature any chelate or unidentate geometries, in complete agreement with the ML results. Furthermore, the results of a coordination analysis of these DFT-optimized geometries are in good quantitative agreement with the results of the ML force field simulations.

The relative fractions of bridging *vs.* tilted-bridging geometries can be estimated by clustering the $\{r_2, r_3\}$ data. Using the k-means algorithm as implemented in scikit-learn,[55] we find that on average 37% of ligands adopt the bridging geometry while the remaining 63% can be categorized as tilted-bridges; see Section S2.2 for details. We also observe that some bridging structures in our simulations appear to be stabilised by an additional Pb-O interaction with a third lead atom; see Figure S4 for an example of such geometry. Finally, we note that, in our analysis, coordinations in which one of the oxygen atoms bridges two Pb atoms while the other forms no Pb-O bonds would be categorised as a bridge (since $r_1 \sim r_3$) rather than a unidentate type. As discussed in Section S2.1, we find no substantial contributions from such geometries – only around 2% of the ligands possess an oxygen atom that is further than 3 Å from any of the Pb atoms.

In Figure 3(a), we plot the Pb-O and Pb-C distribution functions; these support the conclusions discussed above. In the Pb-O distribution function, we observe a broad peak centered around 2.5 Å which shows the range of accessible Pb-O interaction lengths. The very wide peak around 4-4.5 Å corresponds to the distance between the oxygen atoms and

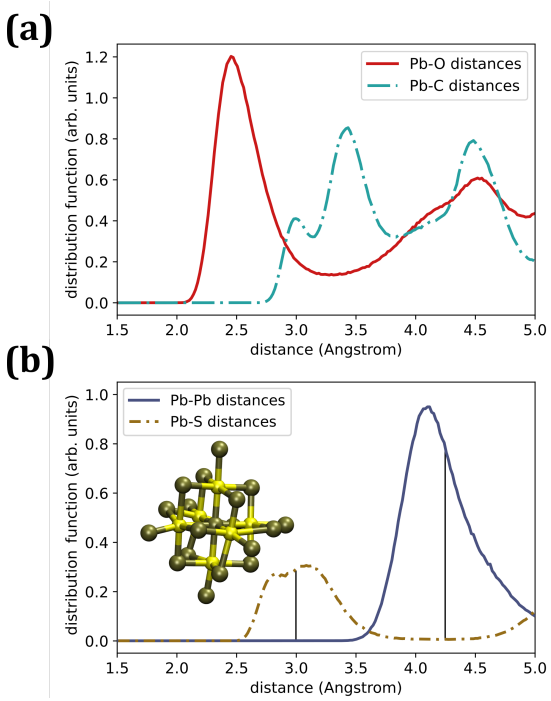

Figure 3: (a) Pb-ligand separations: Pb-O and Pb-C distribution functions. (b) Intra-QD interfacial separations: Pb-S and Pb-Pb distribution functions. The vertical lines indicate the relevant separations in an idealised PbS crystal. Inset: nanocrystal geometry from a 300 K simulation (ligands not shown for clarity).

the neighbouring Pb atoms, including those across the (tilted) carboxylate bridge. In the Pb-C distribution function, we find two peaks at around 3.0 and 3.5 Å. The former can be identified as the shorter of the two Pb-C distances in a tilted-bridge geometry, *c.f.* Figure 2(a), while the latter corresponds to the Pb-C separation in the bridging coordination and the remaining Pb-C distance in the tilted-bridge. (The peak at around 4.5 Å stems from the carbon atom of the methyl group.)

We also analyze the Pb-Pb and Pb-S distribution functions (for the interfacial lead atoms) which are shown in Figure 3(b). The vertical lines indicate the Pb-Pb and Pb-S distances in an idealised crystal. Both of the considered distributions are broad, indicating the high degree of ligand and Pb atom disorder on the surface of the carboxylate-passivated nanocrystal. The apparent double peak in the Pb-S distribution function, at roughly 2.8 and 3.2 Å, corresponds to the vertex and non-vertex Pb atoms, respectively.

Experimentally, the surface chemistry of nanocrystals passivated with carboxylate ligands

is most frequently investigated using IR spectroscopy.[53,56–60] In particular, the relative positions and the spacings between the symmetric and antisymmetric carboxyl stretches are used to infer the ligand coordination geometry.[61] Based on the broad and highly non-Lorentzian shape of the IR peaks associated with the carboxyl stretches, previous experimental studies of oleate-passivated PbS nanocrystals postulated coexistence of bridging and chelating ligands,[53,57,58] in an apparent contradiction to our results here. We also note here that DFT calculations suggest that bridging and tilted-bridging ligands are expected to yield similar IR signals[56] and the two geometry types are often not discussed separately. To resolve this apparent inconsistency, in the remainder of this work, we focus on evaluating the vibrational spectrum of the considered system.

Broadly speaking, the IR spectra can be estimated in two different ways:[62] one can either (i) perform a static (harmonic) normal mode analysis, as typically implemented in electronic structure software, or (ii) obtain the IR signal from a dipole moment auto-correlation function drawn from an MD simulation. Since the former method neglects any anharmonic effects and, at the same time, becomes computationally demanding for larger systems, the latter method will be discussed here; results of the (harmonic) DFT frequency analysis are presented in Section S3.4. The IR signal is often calculated on single optimized geometries comprising individual ligands bound to a slab or a stoichiometric quantum dot.[15,56] Here, we use the dynamics of the entire nanocrystal system. In doing so, we are able to predict the spectrum for the simulated ensemble of ligand geometries without the need to artificially introduce any broadening.

In order to obtain the necessary dipole moments and avoid computing them with an electronic structure method at every step, we train a new machine learning algorithm to predict the dipole vector for the simulated geometries.[63] We once again use the DeePMD package and DFT data for training with details given in the Methods section. In Figure 4(a), we plot the correlation between the DFT and ML dipole moments for the geometries sampled every 100 ps from the five 3 ns simulations discussed earlier. The algorithm performs very

well with RMSE = 0.40 D, relative to the root-mean-square of dipole vector components of roughly 4.9 D. Using output coordinates and velocities of one of the earlier 300 K simulations as the initial state, we next run a 1 ns constant NVE simulation, computing the ML dipole moment at every step. As shown in Section S3.1, no significant energy drift is observed over the course of this run. The IR signal is subsequently obtained by a Fourier transform of the dipole-dipole correlation function; see Methods.

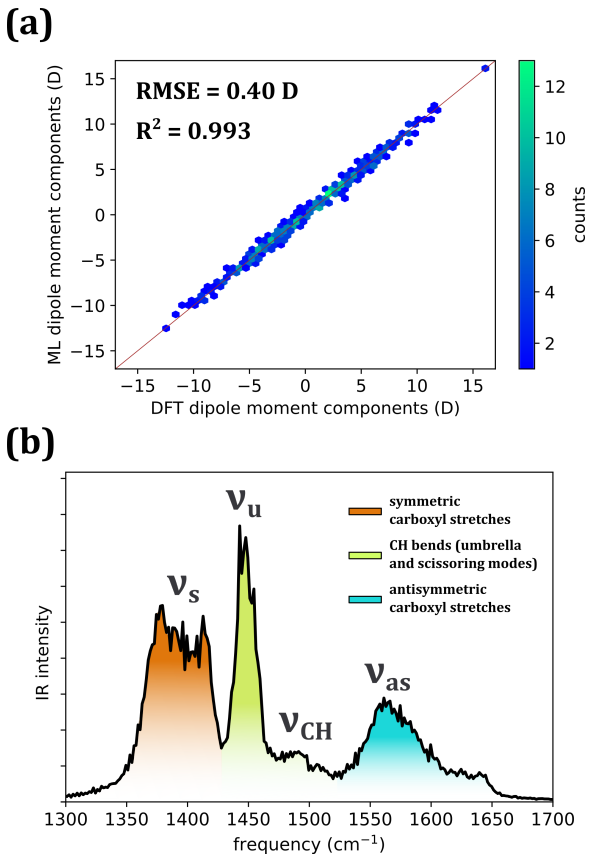

Figure 4: (a) Correlations between the DFT and ML (x, y, z) components of the dipole moment vector for the geometries sampled from the earlier 300 K simulations. (b) IR signal calculated from a 1 ns NVE simulation using the ML dipole moment. Colors indicate the approximate ranges of either CH bends or symmetric/antisymmetric carboxyl stretches.

The resulting IR spectrum in the relevant ligand frequency range is shown in Figure 4(b). We observe a broad peak around $\nu_{\mathrm{s}} \approx$ 1370-1420 cm^{-1} which corresponds to the symmetric stretches within the carboxyl group as well as a band that corresponds to the anti-symmetric stretches at $\nu_{\mathrm{as}} \approx$ 1550-1600 cm^{-1}. The intense signal at around $\nu_{\mathrm{u}} \approx$ 1450 cm^{-1} stems from

the umbrella mode of the methyl group. The remaining CH bends (scissoring modes) give rise to the weak peak at around $\nu_{\mathrm{CH}} \approx 1480$ cm^{-1}.

Alternatively, instead of using the above ML algorithm, the dipole moment and thus the IR spectrum can be calculated using atomic partial charges. We use the previously-calculated ESP partial charges which were averaged for each of the chemically-distinct species including for Pb atoms at the edge, vertex, and in the interior of the QD; see Section S3.2. As shown in Figure S9, the resulting spectrum features virtually identical peak frequencies but markedly different intensities as compared to the IR signal shown in Figure 4(b). This underscores the important limitations of the fixed-partial-charge approach in the present setting. We note however that manipulating these atomic charges allows us to easily identify the (methyl *vs.* carboxyl) origin of each of the vibrational peaks. We also remark here that, as recently demonstrated by Cosseddu and Infante on an example of a carboxylate-passivated CdSe nanocrystal,[22] analytical force fields generally fail to reproduce the correct carboxyl vibrational spectrum.

Very broadly, the IR spectrum shown in Figure 4(b) agrees with the spectra reported for PbS nanocrystals passivated with oleate ligands in which one typically observes the carboxyl symmetric stretches in the region of 1380-1420 cm^{-1}, followed by weak CH bends around 1450 cm^{-1} and the antisymmetric stretches from roughly 1500 to 1560 cm^{-1}.[53,57,58] Some of the main discrepancies between them, such as the presence of the intense 1450 cm^{-1} peak and the higher frequencies of the antisymmetric carboxyl stretches in the simulated spectrum, can be explained by the differences between the IR signatures of the acetate and oleate ligands. As shown in Section S3.5, the very intense 'umbrella' modes seen here are virtually silent in longer carboxylate ligands. Additionally, gas phase DFT calculations suggest that the antisymmetric carboxyl stretch is of a slightly higher frequency in an acetate anion than in its longer homologs. We also note that all of the aforementioned experimental studies considered larger nanocrystals than the one investigated here, although only modest size-dependence of the IR signal is usually observed.[53,57] Importantly, however, our results suggest

that the broad and highly non-Lorentzian character of the carboxyl-stretch lineshapes can result from the wide distributions of the bridging/tilted-bridging geometries and need not indicate their coexistence with chelating ligands.

Lastly, we briefly discuss the results obtained using the FF1 force field in which the entire nanocrystal is frozen in an idealised crystal geometry. As shown in Section S4, we again observe a wide distribution of bridging and tilted-bridging ligands, and a complete lack of chelating geometries. As can be seen in Figure S12, the biggest difference, as compared to the results acquired for a flexible QD surface, is the much smaller ratio of the bridging to tilted-bridging geometries in the case of the frozen nanocrystal. This can be understood by noting that, as shown in Figure 3(b), once the constraints on surface atoms are removed, the typical Pb-Pb spacing on the QD surface decreases to better match the spacing optimal for a carboxylate bridge. This suggests that distortions of the nanocrystal surface can make important contributions to the distribution of ligand geometries.

In summary, we developed and made use of ML force fields to understand the surface chemistry of an ultra small and heavily lead-rich PbS nanocrystal. We have shown that carboxylate ligands passivating the (111) surfaces of the QD adopt a notably broad distribution of bridge and tilted-bridge geometries. Similarly, we have demonstrated that the surface of the passivated nanocrystal is significantly distorted compared to the idealised crystal structure. Our simulations appear to contradict the conventional interpretation of experimental IR studies on PbS quantum dots according to which the non-Lorentzian lineshape is a result of coexistence of chelating and bridging oleate ligands. Although, here, we made use of shorter acetate ligands and the nanocrystal considered is smaller than the ones investigated experimentally, our results suggest that the broad vibrational spectrum can stem from the wide range of accessible (tilted) bridge geometries without invoking another class of structures. Our future efforts will focus on introducing solvation as well as investigating larger quantum dots and bulkier ligands, in order to allow for a clear, direct comparison with experiment. Finally, this work reinforces the view that machine-learned force fields constitute

a powerful tool in the modelling of semiconducting nanocrystals, where traditional analytical partial charge models are clearly challenged. Such studies should advance our understanding of these complex systems and therefore aid in the design of quantum dot-based technologies.

Computational Methods

Unless indicated otherwise, the electronic structure calculations were performed in NWChem 7.0.0.[48] We use the dispersion corrected PBE0-D3 functional[64,65] and the polarization-consistent lanl2dz and 6-31G basis sets throughout for PbS and the remaining light atoms, respectively. The core electrons in Pb and S atoms were accounted for using the corresponding effective core potentials. The starting point for force field training were geometries from a conventional MD simulation obtained using a force field akin to the one used by us previously.[31] The force fields were trained on both the energies and forces with a cut-off of 8 Å. Within DeePMD, we use three hidden layers of size (25, 50, 100) for the embedding net and three (240, 240, 240) hidden layers for the fitting neural network. We followed an iterative scheme[66,67] in which the force field trained on a given set of geometries was used to generate new coordinates for training and validation by propagating geometries from the original set; see Section S1 for details. This cycle is repeated until the energies stabilize, MAE on energy drops below 1 meV/atom for the validation set, and the force field appears stable. Overall, for FF1, we used 7400 geometries for training and 845 for validation. For FF2, we used 8961 geometries for training and 994 for validation.

The constant-temperature MD was implemented using the Langevin BAOAB algorithm[68] with a time step of 1 fs and the damping coefficient of 0.5 ps^{-1}; geometries were saved every 0.5 ps. For the NVE simulations, we use the Verlet algorithm with a time step of 1 fs.

The IR signal obtained from the NVE simulations was calculated by performing a Fourier

transform of the classical dipole-dipole correlation function[69]

$$I(\omega) \propto \int_{-\infty}^{\infty} \mathrm{d}t \, \langle \dot{\mu}(\tau)\dot{\mu}(t-\tau)\rangle_\tau \, e^{\mathrm{i}\omega t}, \tag{1}$$

where $\dot{\mu}(t)$ is the derivative of the dipole moment at time t and $\langle\cdot\rangle_\tau$ denotes an ensemble average over τ. The above expression makes use of the harmonic quantum correction factor[70] which has been shown to satisfy the fluctuation-dissipation theorem.[71]

To machine-learn the dipole moment obtained from DFT calculations, we again used the DeePMD framework with three hidden layers of size (25, 50, 100) for the embedding net and three (100, 100, 100) hidden layers for the fitting neural network. The training was performed for 1.2×10^5 steps with an exponentially decaying learning rate (from 0.01 to 3.51×10^{-8}). 5780 geometries, with corresponding dipole moments, were used for training and 200 for validation.

All 3D visualisations were rendered using VMD.[72]

Acknowledgement

The authors thank Benjamin Levine for helpful discussions. This work was supported by the Center for Adapting Flaws into Features, an NSF Center for Chemical Innovation supported by grant CHE-2124983 and by the Big-Data Private-Cloud Research Cyberinfrastructure MRI award funded by the NSF under grant CNS-1338099 and by Rice University's Center for Research Computing (CRC).

Supporting Information Available

Details of the ML training procedure; additional results supporting the coordination analysis; additional IR data and details of the IR evaluation procedures; results of ESP partial charge analysis; simulation results obtained using the FF1 force field.

Data availability statement

The data that support the findings of this study are openly available at the following URL: `https://figshare.com/articles/dataset/MD_data_and_force_fields_for_MD_simulations_of_a_passivated_PbS_nanocrystal/22822334`

References

(1) Hines, M. A.; Scholes, G. D. Colloidal PbS nanocrystals with size-tunable near-infrared emission: observation of post-synthesis self-narrowing of the particle size distribution. *Adv. Mater.* **2003**, *15*, 1844–1849.

(2) Bakueva, L.; Gorelikov, I.; Musikhin, S.; Zhao, X. S.; Sargent, E. H.; Kumacheva, E. PbS quantum dots with stable efficient luminescence in the near-IR spectral range. *Adv. Mater.* **2004**, *16*, 926–929.

(3) Calvin, J. J.; Brewer, A. S.; Alivisatos, A. P. The role of organic ligand shell structures in colloidal nanocrystal synthesis. *Nat. Synth.* **2022**, *1*, 127–137.

(4) Yin, Y.; Alivisatos, A. P. Colloidal nanocrystal synthesis and the organic–inorganic interface. *Nature* **2005**, *437*, 664–670.

(5) Choi, H.; Ko, J.-H.; Kim, Y.-H.; Jeong, S. Steric-hindrance-driven shape transition in PbS quantum dots: understanding size-dependent stability. *J. Am. Chem. Soc.* **2013**, *135*, 5278–5281.

(6) Krause, M. M.; Kambhampati, P. Linking surface chemistry to optical properties of semiconductor nanocrystals. *Phys. Chem. Chem. Phys.* **2015**, *17*, 18882–18894.

(7) Kroupa, D. M.; Vörös, M.; Brawand, N. P.; McNichols, B. W.; Miller, E. M.; Gu, J.; Nozik, A. J.; Sellinger, A.; Galli, G.; Beard, M. C. Tuning colloidal quantum dot band

edge positions through solution-phase surface chemistry modification. *Nat. Commun.* **2017**, *8*, 15257.

(8) Brown, P. R.; Kim, D.; Lunt, R. R.; Zhao, N.; Bawendi, M. G.; Grossman, J. C.; Bulovic, V. Energy level modification in lead sulfide quantum dot thin films through ligand exchange. *ACS Nano* **2014**, *8*, 5863–5872.

(9) Giansante, C.; Infante, I.; Fabiano, E.; Grisorio, R.; Suranna, G. P.; Gigli, G. "Darker-than-black" PbS quantum dots: enhancing optical absorption of colloidal semiconductor nanocrystals via short conjugated ligands. *J. Am. Chem. Soc.* **2015**, *137*, 1875–1886.

(10) Harris, R. D.; Bettis Homan, S.; Kodaimati, M.; He, C.; Nepomnyashchii, A. B.; Swenson, N. K.; Lian, S.; Calzada, R.; Weiss, E. A. Electronic processes within quantum dot-molecule complexes. *Chem. Rev.* **2016**, *116*, 12865–12919.

(11) Bender, J. A.; Raulerson, E. K.; Li, X.; Goldzak, T.; Xia, P.; Van Voorhis, T.; Tang, M. L.; Roberts, S. T. Surface states mediate triplet energy transfer in nanocrystal–acene composite systems. *J. Am. Chem. Soc.* **2018**, *140*, 7543–7553.

(12) Boles, M. A.; Ling, D.; Hyeon, T.; Talapin, D. V. The surface science of nanocrystals. *Nat. Mater.* **2016**, *15*, 141–153.

(13) Kilina, S.; Ivanov, S.; Tretiak, S. Effect of surface ligands on optical and electronic spectra of semiconductor nanoclusters. *J. Am. Chem. Soc.* **2009**, *131*, 7717–7726.

(14) Padgaonkar, S.; Eckdahl, C. T.; Sowa, J. K.; López-Arteaga, R.; Westmoreland, D. E.; Woods, E. F.; Irgen-Gioro, S.; Nagasing, B.; Seideman, T.; Hersam, M. C. et al. Light-triggered switching of quantum dot photoluminescence through excited-state electron transfer to surface-bound photochromic molecules. *Nano Lett.* **2021**, *21*, 854–860.

(15) Abuelela, A. M.; Mohamed, T. A.; Prezhdo, O. V. DFT simulation and vibrational

analysis of the IR and Raman spectra of a CdSe quantum dot capped by methylamine and trimethylphosphine oxide ligands. *J. Phys. Chem. C* **2012**, *116*, 14674–14681.

(16) McIsaac, A. R.; Goldzak, T.; Van Voorhis, T. It is a trap!: The effect of self-healing of surface defects on the excited states of CdSe nanocrystals. *J. Phys. Chem. Lett.* **2023**, *14*, 1174–1181.

(17) Morris-Cohen, A. J.; Aruda, K. O.; Rasmussen, A. M.; Canzi, G.; Seideman, T.; Kubiak, C. P.; Weiss, E. A. Controlling the rate of electron transfer between a quantum dot and a tri-ruthenium molecular cluster by tuning the chemistry of the interface. *Phys. Chem. Chem. Phys.* **2012**, *14*, 13794–13801.

(18) Zherebetskyy, D.; Scheele, M.; Zhang, Y.; Bronstein, N.; Thompson, C.; Britt, D.; Salmeron, M.; Alivisatos, P.; Wang, L.-W. Hydroxylation of the surface of PbS nanocrystals passivated with oleic acid. *Science* **2014**, *344*, 1380–1384.

(19) Argeri, M.; Fraccarollo, A.; Grassi, F.; Marchese, L.; Cossi, M. Density functional theory modeling of PbSe nanoclusters: effect of surface passivation on shape and composition. *J. Phys. Chem. C* **2011**, *115*, 11382–11389.

(20) Koposov, A. Y.; Cardolaccia, T.; Albert, V.; Badaeva, E.; Kilina, S.; Meyer, T. J.; Tretiak, S.; Sykora, M. Formation of assemblies comprising Ru–polypyridine complexes and CdSe nanocrystals studied by ATR-FTIR spectroscopy and DFT modeling. *Langmuir* **2011**, *27*, 8377–8383.

(21) Rabani, E. Structure and electrostatic properties of passivated CdSe nanocrystals. *J. Chem. Phys.* **2001**, *115*, 1493–1497.

(22) Cosseddu, S.; Infante, I. Force field parametrization of colloidal CdSe nanocrystals using an adaptive rate Monte Carlo optimization algorithm. *J. Chem. Theory Comput.* **2017**, *13*, 297–308.

(23) Schapotschnikow, P.; Hommersom, B.; Vlugt, T. J. Adsorption and binding of ligands to CdSe nanocrystals. *J. Phys. Chem. C* **2009**, *113*, 12690–12698.

(24) Schapotschnikow, P.; Van Huis, M. A.; Zandbergen, H. W.; Vanmaekelbergh, D.; Vlugt, T. J. Morphological transformations and fusion of PbSe nanocrystals studied using atomistic simulations. *Nano Lett.* **2010**, *10*, 3966–3971.

(25) Geva, N.; Shepherd, J. J.; Nienhaus, L.; Bawendi, M. G.; Van Voorhis, T. Morphology of passivating organic ligands around a nanocrystal. *J. Phys. Chem. C* **2018**, *122*, 26267–26274.

(26) De Nolf, K.; Cosseddu, S. M.; Jasieniak, J. J.; Drijvers, E.; Martins, J. C.; Infante, I.; Hens, Z. Binding and packing in two-component colloidal quantum dot ligand shells: linear versus branched carboxylates. *J. Am. Chem. Soc.* **2017**, *139*, 3456–3464.

(27) De Roo, J.; Yazdani, N.; Drijvers, E.; Lauria, A.; Maes, J.; Owen, J. S.; Van Driessche, I.; Niederberger, M.; Wood, V.; Martins, J. C. et al. Probing solvent–ligand interactions in colloidal nanocrystals by the NMR line broadening. *Chem. Mater.* **2018**, *30*, 5485–5492.

(28) Voznyy, O. Mobile surface traps in CdSe nanocrystals with carboxylic acid ligands. *J. Phys. Chem. C* **2011**, *115*, 15927–15932.

(29) Shi, G.; Wang, H.; Zhang, Y.; Cheng, C.; Zhai, T.; Chen, B.; Liu, X.; Jono, R.; Mao, X.; Liu, Y. et al. The effect of water on colloidal quantum dot solar cells. *Nat. Commun.* **2021**, *12*, 4381.

(30) Andrejevic, J.; Stevenson, J.; Clancy, P. Simple molecular reactive force field for metal–organic synthesis. *J. Chem. Theory Comput.* **2016**, *12*, 825–838.

(31) Cadena, D. M.; Sowa, J. K.; Cotton, D. E.; Wight, C. D.; Hoffman, C. L.; Wagner, H. R.; Boette, J. T.; Raulerson, E. K.; Iverson, B. L.; Rossky, P. J. et al. Aggregation of charge

acceptors on nanocrystal surfaces alters rates of photoinduced electron transfer. *J. Am. Chem. Soc.* **2022**, *144*, 22676–22688.

(32) Fan, Z.; Koster, R. S.; Wang, S.; Fang, C.; Yalcin, A. O.; Tichelaar, F. D.; Zandbergen, H. W.; Van Huis, M. A.; Vlugt, T. J. A transferable force field for CdS-CdSe-PbS-PbSe solid systems. *J. Chem. Phys.* **2014**, *141*, 244503.

(33) Voznyy, O.; Mokkath, J. H.; Jain, A.; Sargent, E. H.; Schwingenschlögl, U. Computational study of magic-size CdSe clusters with complementary passivation by carboxylic and amine ligands. *J. Phys. Chem. C* **2016**, *120*, 10015–10019.

(34) Behler, J.; Parrinello, M. Generalized neural-network representation of high-dimensional potential-energy surfaces. *Phys. Rev. Lett.* **2007**, *98*, 146401.

(35) Behler, J. Perspective: Machine learning potentials for atomistic simulations. *J. Chem. Phys.* **2016**, *145*, 170901.

(36) Unke, O. T.; Chmiela, S.; Sauceda, H. E.; Gastegger, M.; Poltavsky, I.; Schütt, K. T.; Tkatchenko, A.; Müller, K.-R. Machine learning force fields. *Chem. Rev.* **2021**, *121*, 10142–10186.

(37) Poltavsky, I.; Tkatchenko, A. Machine learning force fields: Recent advances and remaining challenges. *J. Phys. Chem. Lett.* **2021**, *12*, 6551–6564.

(38) Deringer, V. L.; Caro, M. A.; Csányi, G. Machine learning interatomic potentials as emerging tools for materials science. *Adv. Mater.* **2019**, *31*, 1902765.

(39) Dajnowicz, S.; Agarwal, G.; Stevenson, J. M.; Jacobson, L. D.; Ramezanghorbani, F.; Leswing, K.; Friesner, R. A.; Halls, M. D.; Abel, R. High-dimensional neural network potential for liquid electrolyte simulations. *J. Phys. Chem. B* **2022**, *126*, 6271–6280.

(40) Wen, B.; Calegari Andrade, M. F.; Liu, L.-M.; Selloni, A. Water dissociation at the

water–rutile TiO2 (110) interface from ab initio-based deep neural network simulations. *Proc. Natl. Acad. Sci. U.S.A.* **2023**, *120*, e2212250120.

(41) Gartner III, T. E.; Zhang, L.; Piaggi, P. M.; Car, R.; Panagiotopoulos, A. Z.; Debenedetti, P. G. Signatures of a liquid–liquid transition in an ab initio deep neural network model for water. *Proc. Natl. Acad. Sci. U.S.A.* **2020**, *117*, 26040–26046.

(42) Winter, G.; Gómez-Bombarelli, R. Simulations with machine learning potentials identify the ion conduction mechanism mediating non-Arrhenius behavior in LGPS. *J. Phys.: Energy* **2023**, *5*, 024004.

(43) Quaranta, V.; Hellström, M.; Behler, J. Proton-transfer mechanisms at the water–ZnO interface: The role of presolvation. *J. Phys. Chem. Lett.* **2017**, *8*, 1476–1483.

(44) Kim, D.; Kim, D.-H.; Lee, J.-H.; Grossman, J. C. Impact of stoichiometry on the electronic structure of PbS quantum dots. *Phys. Rev. Lett.* **2013**, *110*, 196802.

(45) Beygi, H.; Sajjadi, S. A.; Babakhani, A.; Young, J. F.; van Veggel, F. C. Surface chemistry of as-synthesized and air-oxidized PbS quantum dots. *Appl. Surf. Sci.* **2018**, *457*, 1–10.

(46) Kessler, M. L.; Dempsey, J. L. Mapping the topology of PbS nanocrystals through displacement isotherms of surface-bound metal oleate complexes. *Chem. Mater.* **2020**, *32*, 2561–2571.

(47) Imperiale, C. J.; Green, P. B.; Hasham, M.; Wilson, M. W. Ultra-small PbS nanocrystals as sensitizers for red-to-blue triplet-fusion upconversion. *Chem. Sci.* **2021**, *12*, 14111–14120.

(48) Apra, E.; Bylaska, E. J.; De Jong, W. A.; Govind, N.; Kowalski, K.; Straatsma, T. P.; Valiev, M.; van Dam, H. J.; Alexeev, Y.; Anchell, J. et al. NWChem: Past, present, and future. *J. Chem. Phys.* **2020**, *152*, 184102.

(49) Wang, H.; Zhang, L.; Han, J.; Weinan, E. DeePMD-kit: A deep learning package for many-body potential energy representation and molecular dynamics. *Comput. Phys. Commun.* **2018**, *228*, 178–184.

(50) Zhang, L.; Han, J.; Wang, H.; Car, R.; Weinan, E. Deep potential molecular dynamics: a scalable model with the accuracy of quantum mechanics. *Phys. Rev. Lett.* **2018**, *120*, 143001.

(51) Zeng, J.; Zhang, D.; Lu, D.; Mo, P.; Li, Z.; Chen, Y.; Rynik, M.; Huang, L.; Li, Z.; Shi, S. et al. DeePMD-kit v2: A software package for deep potential models. *arXiv* **2023**, DOI:10.48550/arXiv.2304.09409.

(52) Liu, J.-C.; Luo, L.; Xiao, H.; Zhu, J.; He, Y.; Li, J. Metal affinity of support dictates sintering of gold catalysts. *J. Am. Chem. Soc.* **2022**, *144*, 20601–20609.

(53) Cass, L. C.; Malicki, M.; Weiss, E. A. The chemical environments of oleate species within samples of oleate-coated PbS quantum dots. *Anal. Chem.* **2013**, *85*, 6974–6979.

(54) Cosseddu, S.; Pascazio, R.; Giansante, C.; Manna, L.; Infante, I. Ligand dynamics on the surface of CdSe nanocrystals. *Nanoscale* **2023**, *15*, 7410–7419.

(55) Pedregosa, F.; Varoquaux, G.; Gramfort, A.; Michel, V.; Thirion, B.; Grisel, O.; Blondel, M.; Prettenhofer, P.; Weiss, R.; Dubourg, V. et al. Scikit-learn: machine learning in python. *J. Mach. Learn. Res.* **2011**, *12*, 2825–2830.

(56) Zhang, J.; Zhang, H.; Cao, W.; Pang, Z.; Li, J.; Shu, Y.; Zhu, C.; Kong, X.; Wang, L.; Peng, X. Identification of facet-dependent coordination structures of carboxylate ligands on CdSe nanocrystals. *J. Am. Chem. Soc.* **2019**, *141*, 15675–15683.

(57) Kennehan, E. R.; Munson, K. T.; Doucette, G. S.; Marshall, A. R.; Beard, M. C.; Asbury, J. B. Dynamic ligand surface chemistry of excited PbS quantum dots. *J. Phys. Chem. Lett.* **2020**, *11*, 2291–2297.

(58) Peters, J. L.; de Wit, J.; Vanmaekelbergh, D. Sizing curve, absorption coefficient, surface chemistry, and aliphatic chain structure of PbTe nanocrystals. *Chem. Mater.* **2019**, *31*, 1672–1680.

(59) Peters, J. L.; Van Der Bok, J.; Hofmann, J. P.; Vanmaekelbergh, D. Hybrid oleate–iodide ligand shell for air-stable PbSe nanocrystals and superstructures. *Chem. Mater.* **2019**, *31*, 5808–5815.

(60) Cros-Gagneux, A.; Delpech, F.; Nayral, C.; Cornejo, A.; Coppel, Y.; Chaudret, B. Surface chemistry of InP quantum dots: a comprehensive study. *J. Am. Chem. Soc.* **2010**, *132*, 18147–18157.

(61) Deacon, G.; Phillips, R. Relationships between the carbon-oxygen stretching frequencies of carboxylato complexes and the type of carboxylate coordination. *Coord. Chem. Rev.* **1980**, *33*, 227–250.

(62) Thomas, M.; Brehm, M.; Fligg, R.; Vöhringer, P.; Kirchner, B. Computing vibrational spectra from ab initio molecular dynamics. *Phys. Chem. Chem. Phys.* **2013**, *15*, 6608–6622.

(63) Gastegger, M.; Behler, J.; Marquetand, P. Machine learning molecular dynamics for the simulation of infrared spectra. *Chem. Sci.* **2017**, *8*, 6924–6935.

(64) Adamo, C.; Barone, V. Toward reliable density functional methods without adjustable parameters: The PBE0 model. *J. Chem. Phys.* **1999**, *110*, 6158–6170.

(65) Grimme, S.; Antony, J.; Ehrlich, S.; Krieg, H. A consistent and accurate ab initio parametrization of density functional dispersion correction (DFT-D) for the 94 elements H-Pu. *J. Chem. Phys.* **2010**, *132*, 154104.

(66) Sosso, G. C.; Miceli, G.; Caravati, S.; Behler, J.; Bernasconi, M. Neural network interatomic potential for the phase change material GeTe. *Phys. Rev. B* **2012**, *85*, 174103.

(67) Deringer, V. L.; Csányi, G. Machine learning based interatomic potential for amorphous carbon. *Phys. Rev. B* **2017**, *95*, 094203.

(68) Leimkuhler, B.; Matthews, C. Robust and efficient configurational molecular sampling via Langevin dynamics. *J. Chem. Phys.* **2013**, *138*, 174102.

(69) Iftimie, R.; Minary, P.; Tuckerman, M. E. Ab initio molecular dynamics: Concepts, recent developments, and future trends. *Proc. Natl. Acad. Sci. U.S.A.* **2005**, *102*, 6654–6659.

(70) Bader, J. S.; Berne, B. Quantum and classical relaxation rates from classical simulations. *J. Chem. Phys.* **1994**, *100*, 8359–8366.

(71) Ramırez, R.; López-Ciudad, T.; Kumar P, P.; Marx, D. Quantum corrections to classical time-correlation functions: Hydrogen bonding and anharmonic floppy modes. *J. Chem. Phys.* **2004**, *121*, 3973–3983.

(72) Humphrey, W.; Dalke, A.; Schulten, K. VMD: visual molecular dynamics. *J. Mol. Graph.* **1996**, *14*, 33–38.